

# Characterization of viscoelastic properties of normal and cancerous human breast cells using a confining microchannel

Shuhuan Hu<sup>1</sup> · Raymond H. W. Lam<sup>1,2,3,4</sup>

Received: 8 January 2017 / Accepted: 16 March 2017  
© Springer-Verlag Berlin Heidelberg 2017

**Abstract** Biomechanical properties have been revealed as potential biomarkers for distinguishing cancer cells from normal cells. In this work, we report a novel technique using a confining microchannel for biomechanical phenotyping for floating human cells, including one normal breast cell line (MCF-10A) and two breast cancer cell lines (MCF-7 and MDA-MB-231). The floating cells move under a defined pressure profile along the microchannel, in which the cells deform dynamically under compression by the channel sidewalls. We adopt the Hertz and Tataro model to convert deformed cell shapes to cell diameters and transient stress–strain ratios. By further considering cell viscoelasticity as a standard linear solid model, we compute for whole-cell viscosity, and instantaneous and relaxed moduli. Our results show that the selected cell types have significant different viscoelastic properties. We further implement cell-type classification based on the multiple parametric biomechanical cell properties with reasonable sensitivities (>65%). Applications of the confining microchannel can be further extended for high-throughput, continuous-flow deep phenotyping of rare cells by surface functionalization for both biomechanical and biochemical biomarkers for more comprehensive and promising cell characterization.

**Keywords** Microfluidic · Cancer · Viscoelasticity · Viscosity · Elasticity

## 1 Introduction

Biomechanical properties of single cells have been recognized as important phenotypes and indicators of any mechanistic or genetic alternations such as cancer. For instance, a metastasis-suppressing gene (BRMS1) (Shevde and Welch 2003) can induce elasticity of a highly metastatic breast cancer cell line (MDA-MB-435) (Wu et al. 2010). Though cancer cells have long been studied and well-recognized, detailed contributions of their biomechanical properties in cancer progression, e.g., invasion, remains obscure (Swaminathan et al. 2011). Considering that genetic and molecular hallmarks of cancer are often heterogeneous and inconsistent/confusing even for the same cancer type, viscoelastic properties of cancer cells during the disease progression have demonstrated to be potentially as promising as many biochemical aspects (Lekka et al. 2012). In fact, cell viscoelasticity have been found to be distinct among the normal, benign and malignant tumor cells (Suresh 2007). It has been widely reported that more deformable cancer cells tend to reflect their higher invasive capability and metastatic potential in general (Chambers et al. 2002). Metastatic tumor cells are responsible for the major deaths of cancer patients (Chaffer and Weinberg 2011; Steeg 2006). Therefore, cell classification technologies based on biomechanical factors such as the whole-cell deformability have caught the eyes of researchers as potential biomarkers for cancer staging and even early detection (Hur et al. 2011).

Cancer cells exhibit viscoelastic properties as soft materials (Fung 2013), largely contributed from the constitutive

✉ Raymond H. W. Lam  
rhwlam@cityu.edu.hk

<sup>1</sup> Department of Mechanical and Biomedical Engineering, City University of Hong Kong, Kowloon Tong, Hong Kong

<sup>2</sup> Centre for Robotics and Automation, City University of Hong Kong, Kowloon Tong, Hong Kong

<sup>3</sup> Centre for Biosystems, Neuroscience, and Nanotechnology, City University of Hong Kong, Kowloon Tong, Hong Kong

<sup>4</sup> City University of Hong Kong Shenzhen Research Institute, Shenzhen, China

viscoelastic intracellular components, e.g., cross-linked cytoskeletal networks of microfilaments, microtubules, and intermediate filaments (Bao and Suresh 2003) contained in an interstitial viscous liquid (Fletcher and Mullins 2010; Moeendarbary et al. 2013). Cell viscoelasticity can also be partially affected by other factors such as repeated breakages and reforms of weak bonds around the fibers (Ateshian 2015; Hoffman et al. 2011), and frictions between the fibers and the interstitial liquid (Gittes and MacKintosh 1998). Hence, a more comprehensive description of the mechanical cell properties should include both ‘solid’ and ‘fluidic’ perspectives (Suresh 2007) as a time-varying stress–strain relation of the whole-cell body. Since the past decades, researchers have adopted a number of techniques for the biomechanical phenotyping, such as atomic force microscopy (AFM) (Ketene et al. 2012), magnetic bead microrheometry (MBM) (Bausch et al. 2001), and micropipette aspiration (Trickey et al. 2006). Other than the relatively complex setup and operations, AFM and MBM measured only the biomechanical properties for local sites at adherent cells growing in vitro, which might reveal only a limited relevance between measurements and the whole-cell characteristics of floating cells in bio-samples. Micropipette aspiration has a very low throughput because of the time consuming aspiration-releasing processes operated on a single cell (Kim et al. 2009); and it has been shown to cause irreversible damages to the cells (Tan et al. 2008), restricting any downstream cell phenotyping processes and analyses.

Microfluidics has been successfully applied for developing effective micro-tools for maintaining viability (Lei et al. 2012) and quantifying mechanical behaviors of floating rare cells (Byun et al. 2013; Gossett et al. 2012) together with a higher throughput and extended operation functionality such as the deformability-based cell separation (Zhang et al. 2012). Cancer patients’ blood containing circulating tumor cells (CTCs) has been widely used as an effective ‘liquid biopsy’ for metastasis diagnosis (Alix-Panabières and Pantel 2013). For example, Negrath et al. (2007) introduced a microfluidic device achieving efficient isolation of CTCs from such liquid biopsy. Further, microfluidics has been applied to conduct biophysical phenotyping of clinical liquid biopsy samples (Chen et al. 2013; Maheswaran et al. 2008; Wang et al. 2007). Dudani et al. (2013) utilized hydraulic forces from vortex flows to select floating rare cells and to measure their deformability (Sollier et al. 2014). Studies have been reported other biophysical phenotyping and cell sorting techniques in microfluidics by inducing physical forces, such as optical forces (Huang et al. 2013; Wang et al. 2005; Yang et al. 2015), flexible thin film stretching (Hohne et al. 2009), acoustic forces (Li et al. 2015) and magnetic forces (Inglis et al. 2004; Kong et al. 2015). However, there is only a few microfluidic

devices developed for measuring the viscoelasticity of floating cells, which can provide further biophysical cell properties as additional promising biomarkers. Sawetzki et al. reported the application of flow cytometry to reveal viscoelasticity related parameters, yet the integration with other biochemical sensing (Lei and Butt 2010; Lin et al. 2014) is challenging because of the absence of contact with any functional device surfaces. To achieve a microfluidic for quantifying both biophysical and biochemical cell properties, design of the flow channels is particularly critical for successful and promising cell viscoelasticity measurement (Tran et al. 2016; Warren et al. 2016), which includes factors such as a representative model for the cell biomechanics under well-defined applied forces, microstructures and flow conditions.

In this manuscript, we devise a simple yet reliable microfluidic strategy for measuring cell viscoelasticity using a confining microchannel fabricated by traditional soft lithography (Xia and Whitesides 1998). Through detailed analysis on the fluidic conditions around a floating cell captured in the microchannel with defined dimensions, we can convert the transient deformation of a cell under the surrounding hydraulic pressure profile to its biomechanical properties, described by a standard linear solid (SLS) model (Li et al. 1995) with elasticity and viscosity coefficients. We further implement classification of normal and cancerous human breast cell types based on their biomechanical properties, which has great potentials in applications such as cell biomechanics study and cancer diagnosis.

## 2 Model

To obtain feasible dimensions of a confining channel for the cell viscoelasticity measurement, we first consider a cell flowing into the microchannel, in which the resultant cell deformation was caused by compression from confining channel sidewalls (Liu et al. 2015). Here, we focus on measurement of the cells with a spherical shape in suspension, e.g., CTCs and lymphocytes. The confining channel was configured as shown in Fig. 1a, with the inlet width  $W_{in}$ , outlet width  $W_{out}$ , channel height  $H_{channel}$  and channel length  $L_{channel}$ , inducing an angle of confinement  $\theta$  ( $=\tan^{-1}[(W_{out} - W_{in})/(2L_{channel})]$ ).  $W_{out}$  should be set smaller than the cell diameter  $D_{cell}$ , such that the cell contacts channel side walls and deforms inside the confining channels.  $H_{channel}$  should be designed to be sufficiently large for avoiding the contacts between cells and the upper and lower channel surfaces. The friction coefficient between the confining channel walls and cancer cell membranes can be reduced from 0.3 (Luo et al. 2014) to  $<0.008$  (Chawla et al. 2009) by coating a hydrophobic poloxamer onto the channel walls, and therefore we shall ignore the

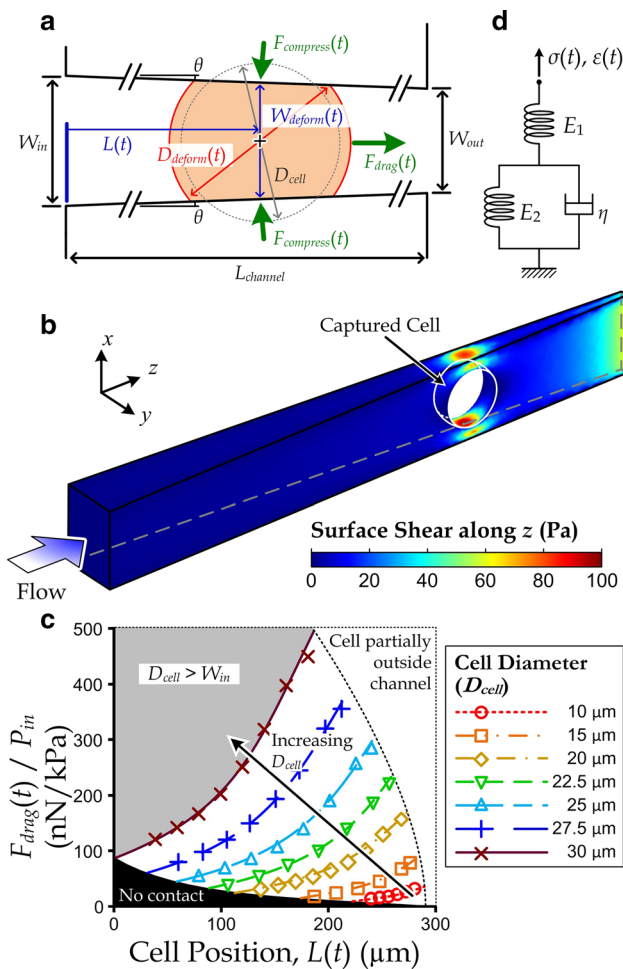


**Fig. 1** **a** Free body diagram showing a cell settling and deforming ( $W_{deform}(t)$ : width of the deformed cell;  $D_{deform}(t)$ : diameter of the deformed cell body) inside a confining channel at a transient position  $L(t)$  as a function of contact time  $t$  under a drag force  $F_{drag}(t)$  along the channel, generating compressive force  $F_{compress}(t)$  acting on the cell by channel sidewalls. **b** Sample simulation result of the surface shear stress in the flow direction of a confining channel containing a deformed cell ( $D_{cell} = 25 \mu\text{m}$ ) at  $L = 210 \mu\text{m}$  along under a driving pressure of 1 kPa. **c** Simulated drag force  $F_{drag}(t)$  acting on a trapped cell per unit inlet hydraulic gage pressure ( $P_{in}$ ) as a function of cell diameter  $D_{cell}$  and  $L(t)$ . **d** Configuration of the standard linear solid (SLS) model describing the cell viscoelastic properties

friction effects. The compressive force  $F_{compress}$  causing cell deformation can be then approximated as  $F_{compress} \approx F_{drag}/(2\sin\theta)$ , where  $F_{drag}$  is the effective drag force acting on the deformed cell under the driving pressure. Due to the fact cells have viscoelasticity properties (Bausch et al. 1999), the cell position  $L(t)$ , defined as the distance between confining channel entrance and cell position, is a function of time  $t$ , counted from the moment the cell in contact with the side walls.

It is reasonable to assume the cell surfaces in contact with confining channel walls to be planar and the

exposed surfaces as spherical within a compression length of  $\sim 20\%$  (Liu et al. 1998). If we further set the confining angle  $\theta$  small enough (e.g.,  $<3^\circ$ ), the deformed cell shape at different contact time  $t$  can then be simplified as a sphere with a diameter of  $D_{deform}(t)$  with its top and bottom roofs each chopped for a length of  $(D_{cell} - W_{deform}(t))/2$ , where  $W_{deform}(t)$  was the cell width at the position  $L(t)$ , with  $W_{deform}(t) = W_{out} + (W_{in} - W_{out})L(t)/L_{channel}$ . Assuming also an negligible volumetric change,  $D_{deform}(t)$  has the following relation (Liu 2006):

$$D_{deform}(t) \approx \sqrt{\frac{2D_{cell}^3}{3W_{deform}(t)} + \frac{W_{deform}^2(t)}{3}} \tag{1}$$

To estimate  $F_{drag}$  for an encapsulated cell with different  $D_{cell}$  and  $L(t)$ , we further performed fluidic simulations with commercially available software (COMSOL Multiphysics 4.2) to compute relevant flow characteristics, including flow velocity, stress and hydraulic pressure profiles around a cell located at different positions along a confining channel with dimensions ( $L_{channel}$ ,  $W_{in}$ ,  $W_{out}$  and the channel height  $H_{channel}$ ). In each case of the simulation, we consider the geometry of a single cell captured at a defined position along the confining channel. It should be noted that  $F_{drag}$  is also a function of time  $t$ . The simulated tensile and shear stress profiles of the cell surface were further converted into an effective drag force  $F_{drag}(t)$  acting on a deformed cell along the flow direction. As demonstration, the shear stress profile of a cell captured and deformed along a confining channel is illustrated in Fig. 1b. As the flow is in the regime of very low Reynolds number ( $Re \ll 1$ ),  $F_{drag}(t)$  is proportional to the gage pressure at the channel inlet ( $P_{in}$ ), relative to the pressure at the channel outlet. We have computed and summarized the ratio between  $F_{drag}(t)$  and  $P_{in}$  as a function of  $D_{cell}$  and  $L(t)$  in the confining channel. Importantly, this relation provides a direct mapping of key experimental parameters [i.e.,  $D_{cell}$  and  $L(t)$ ] to  $F_{drag}(t)$ , which can then be computed by the bilinear interpolation using Fig. 1c.

The compressive force  $F_{compress}(t) (\approx F_{drag}(t)/(2\sin\theta))$  would induce a spatial stress profile  $\sigma(x, y, z, t)$  in the cell body. The small angle of confinement  $\theta$  would induce a dominant compressive force over other effects such as the shear stress on the cell deformation. Here, we consider a principle compressive stress  $\sigma_{yy}(x, y, z, t)$ . Further, the integral of  $F_{compress}(t)$  along the  $y$ -direction should be equal to  $\int_{cell} \sigma_{yy}(x, y, z, t)dV$ , which is  $\sigma_{yy}(x, y, z, t)$  integrating over the entire cell body. We consider the whole-cell principle compressive stress  $\sigma(t)$  in the SLS model as the average principle compressive stress over the cell body, i.e.,  $\sigma(t) = \int_{cell} \sigma_{yy}(x, y, z, t)dV/V_{cell}$  where  $V_{cell} (= \pi D_{cell}^3/6)$  is the cell volume. Similarly, the

corresponding whole-cell principle compressive strain  $\varepsilon(t)$  can be defined as  $\varepsilon(t) = \int_{\text{cell}} \varepsilon_{yy}(x, y, z, t) dV / V_{\text{cell}}$ , where  $\varepsilon_{yy}(x, y, z, t)$  is the principle compressive strain along the y-direction.

We adopt the Hertz’s and Tataru’s theories (Zhang et al. 2007) to describe deformation of encapsulated cells, which can be viewed as non-adhesive soft particles compressed by the channel sidewalls. It has been well proven that the Tataru model can represent the nonlinear elasticity under a large deformation ( $\leq 20\%$  compression) in terms of the nominal transverse strain (Liu 2006; Liu et al. 1998). The transient whole-cell compressive stress  $\sigma(t)$  to compressive strain  $\varepsilon(t)$  ratio can be approximated as (Etsion et al. 2005):

$$\frac{\sigma(t)}{\varepsilon(t)} \approx \left[ \frac{3(1 - \nu_{\text{cell}})}{2D_{\text{contact}}(t)} - \frac{(1 - \nu_{\text{cell}})(D_{\text{contact}}^2(t) + 4D_{\text{cell}}^2)}{4\pi(D_{\text{contact}}^2(t) + 4D_{\text{cell}}^2)^{3/2}} + 4\pi D_{\text{cell}}^2 \right] \times \frac{(1 + \nu_{\text{cell}})F_{\text{drag}}(t)}{(D_{\text{cell}} - W_{\text{deform}}(t)) \sin \theta} \tag{2}$$

where  $\nu_{\text{cell}}$  ( $\approx 0.5$ ) is the Poisson’s ratio of the cell body and  $D_{\text{contact}}(t)$  is the diameter of the contact area with either channel sidewall calculated by  $D_{\text{contact}}(t) = [D_{\text{deform}}^2(t) - W_{\text{deform}}^2(t)]^{1/2}$ .

Furthermore, we aim at converting such measurable transient  $\sigma(t)/\varepsilon(t)$  to the key whole-cell viscoelastic parameters, which can reveal the cell status more directly. To characterize mechanical properties of floating cells using the confining microchannel, we adopt a SLS model (Li et al. 1995) as shown in Fig. 1d to describe the cell viscoelasticity. As this SLS model can only capture the linear viscoelastic properties, we should only consider conditions within a limited cell deformation ( $\leq 20\%$  compression). This model contains a ‘spring’ element (elasticity:  $E_1$ ) connected in series with the Kelvin–Voigt, which is formed by another ‘spring’ element (elasticity:  $E_2$ ) and a ‘damper’ element (viscosity:  $\eta$ ) in parallel. We further consider to describe the viscoelastic process under a time-dependent whole-cell strain  $\varepsilon(t)$  (Bausch et al. 1999). The governing equation can be expressed as

$$(E_1 + E_2)\sigma(t) + \eta\dot{\sigma}(t) = E_1E_2\varepsilon(t) + E_1\eta\dot{\varepsilon}(t). \tag{3}$$

In order to solve Eq. 3, the form of  $\sigma(t)$  should be first defined. As shown in Sect. 4 later in this manuscript, it is reasonable to assume that  $\sigma(t)$  conforms an exponentially stabilizing function; thus,  $\sigma(t)$  can be computed based on the Hertz’s and Tataru’s model as

$$\sigma(t) \approx \frac{3F_{\text{drag}}(t)W_{\text{deform}}(t)}{\pi D_{\text{cell}}^3 \sin \theta} = (\sigma_0 - \sigma_s)e^{-t/\tau} + \sigma_s, \tag{4}$$

where  $\sigma_0$  is the stress at  $t = 0$ ,  $\sigma_s$  is the stress when  $t \rightarrow \infty$  and  $\tau$  is the characteristic time constant of the stress variation. The corresponding whole-cell compressive principle

strain  $\varepsilon(t)$  should be another exponentially stabilizing function by solving Eq. 3 using Eq. 4:

$$\varepsilon(t) = \frac{(E_1 + E_2)\tau - \eta}{E_2\tau - \eta} \frac{(\sigma_0 - \sigma_s)}{E_1} e^{-t/\tau} + \left( \frac{1}{E_1} + \frac{1}{E_2} \right) \sigma_s \tag{5}$$

Apparently, when a cell being captured in the channel for  $t \rightarrow \infty$ , the stress/strain ratio ( $\sigma(t)/\varepsilon(t)$ ) is stabilized as expressed as the ‘relaxed modulus’  $E_s$ . According to Eq. 3 or Eqs. 4 and 5,

$$E_s = \lim_{t \rightarrow \infty} \frac{\sigma(t)}{\varepsilon(t)} = \frac{E_1E_2}{E_1 + E_2}. \tag{6}$$

On the other hand, when a cell first contacts with the channel walls at  $t = 0$ , the Kelvin–Voigt component as shown in Fig. 1c can be temporarily considered as a rigid body and hence the ‘instantaneous modulus’ is  $E_1$  (Cheng et al. 2000). Applying  $E_1 = \sigma(t)/\varepsilon(t)$  at  $t = 0$  as described by Eqs. 4 and 5, we can obtain the expression of viscosity coefficient:

$$\eta = \frac{\sigma_0}{\sigma_s} E_2 \tau \tag{7}$$

### 3 Methods

#### 3.1 Fabrication

Fabrication of the confining microchannels is based on the replica molding of elastomeric polydimethylsiloxane (PDMS) (Sylgard-184, Dow Corning, Midland, MI). We fabricated a silicon mold master by patterning a layer of positive photoresist (AZ5214, AZ Electronic Materials, Wiesbaden, Germany), followed by deep reactive ion etching (DRIE, STS Deep Silicon Etcher, Surface Technology Systems, Newport, UK) with a depth of 40  $\mu\text{m}$ , and stripping off the photoresist. We then silanized the mold master with vaporized (tridecafluoro-1,1,2,2-tetrahydrooctyl)-1-trichlorosilane (cat #448931, Sigma-Aldrich, St. Louis, MO) in a vacuum chamber. Afterward, we fabricated the PDMS substrate containing microchannel patterns by the widely used soft lithography procedures. The PDMS substrate was then bonded onto a glass slide (cat #10127101P-G, Citoglas, Jiangsu, China) by oxygen plasma. While the oxygen plasma-treated surfaces were still active, we injected 1% (w/w) a hydrophobic poloxamer pluronic F-127 (Sigma-Aldrich, St. Louis, MO) in water along the device for 30 min to surface treat the inner channel walls to prevent the possible cell attachments.

#### 3.2 Cell culture

Immortal human breast epithelial cells (MCF-10A), breast cancer cells (MCF-7 and MDA-MB-231) were obtained

from ATCC (Manassas, VA). MCF-10A cells were cultured in the Mammary Epithelial Growth Medium (MEGM; CC-3150, Lonza, New York City, NY) added with 0.4% (v/v) bovine pituitary extract (BD, Franklin Lakes, NJ), 0.1% (v/v) human epithelial growth factor (hEGF; Cell Signaling Technology, Beverly, MA), 0.1% (v/v) hydrocortisone (Sigma-Aldrich, St. Louis, MO), 0.1% (v/v) insulin (Sigma-Aldrich) and 0.1% (v/v) of a reagent mixed with 30 mg/ml gentamicin and 15 μg/ml amphotericin (GA-1000, Lonza). MCF-7 cells were cultured in a high-glucose Dulbecco’s modified Eagle’s medium (DMEM; Invitrogen, Carlsbad, CA) with the supplement of 10% fetal bovine serum (Atlanta Biological, Atlanta, GA), 0.5 μg/ml fungizone (Invitrogen, Carlsbad, CA), 5 μg/ml gentamicin (Invitrogen), 100 units/ml penicillin, and 100 μg/ml streptomycin. MDA-MB-231 cells were cultured in DMEM-F12 (Invitrogen) added with 10% fetal bovine serum and 100 units/ml penicillin. All cells were cultured at 37 °C with ~100% humidity and 5% CO<sub>2</sub> in air in an incubator. To extract the cells for experiments, we applied 0.25% trypsin–EDTA in phosphate buffered saline (PBS) to re-suspend the cells, following by centrifuge and replacement of fresh culture media. The cells were then diluted to the target cell density (~4 × 10<sup>4</sup> cells/ml) by adding additional culture media.

**3.3 Simulation**

To obtain the hydraulic forces exerted onto the encapsulated cells, we performed finite element analysis using commercial software (COMSOL Multiphysics 4.2, Burlington, MA, USA) of multiple models with different geometric parameters. Each model represents a confining channel containing a cell with diameter  $D_{cell}$  located at the position  $L$  inside the channel. The corresponding diameter of the deformed cell  $D_{deform}$  is calculated using Eq. 1. Afterward, the flow profile and the stress profile over the cell surface were simulated using the stationary laminar flow module. Then we can obtain the resultant drag force  $F_{drag}$  by integrating the simulated stress profile over the cell surface by considering only the stress component along the channel direction. Apparently  $F_{drag}$  is proportional to the inlet gage pressure  $P_{in}$ ; and therefore this simulation aimed at obtaining the ratio of  $F_{drag}$  and  $P_{in}$  over the encapsulated cell as a function of  $D_{cell}$  and  $L$  as shown in Fig. 1c.

**3.4 Imaging and processing**

We applied a phase-contrast inverted microscope (TE300, Nikon, Tokyo, Japan) equipped with a long-distance 60× magnification objective and an sCMOS microscope camera (Zyla, Andor, Belfast, UK) and a Solid State Drive (SSD) to capture high-resolution time-lapsed images (~570 nm/

pixel) with a rate of 10 fps. We adopted open source image processing software (ImageJ, NIH) to process the microscopic images, e.g., to measure  $L(t)$  and  $D_{deform}(t)$ .

**3.5 Statistics**

$p$  Values were calculated using the Student’s  $t$  test in Excel (Microsoft, Seattle, WA).

**4 Results and discussion**

**4.1 Device configuration**

We have designed and fabricated a microfluidic device for measurement of cell viscoelastic properties (Fig. 2a). Briefly, this device contains a confining microchannel and two bypass channels aside. Surface roughness of the sidewalls should be negligible as indicated in Fig. 2b. The flow region in the device as well as the height of the confining channel ( $H_{channel}$ ) is 50 μm tall. The confining channel length ( $L_{channel}$ ) is 300 μm. The channel has an entrance with a width ( $W_{in}$ ) of 30 μm and an exit with a width ( $W_{out}$ ) of 4 μm. The flow of cell sample is driven by applying a

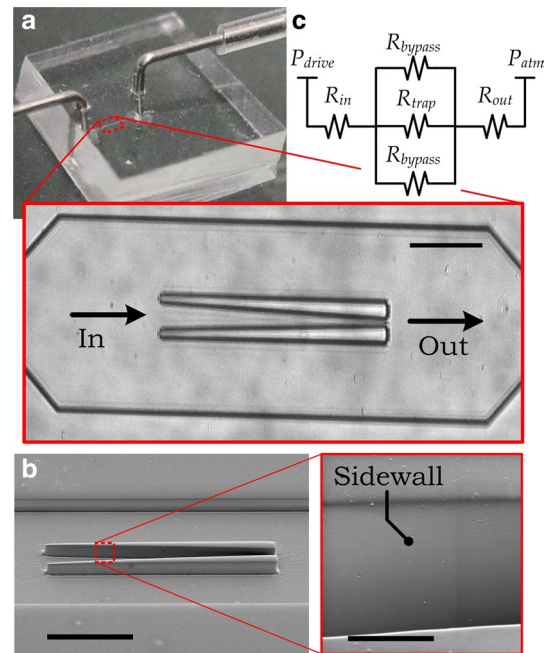


**Fig. 2** a Photograph of a fabricated cell viscoelasticity microcylinder. *Inset* micrograph at the confining microchannel. *Scale bar* 100 μm. b Scanning electron micrograph (SEM) of a fabricated PDMS confining channel before bonding to a glass substrate, viewed from a tilt angle of 45°. *Scale bar* 100 μm. *Inset* inner sidewall of the confining channel. *Scale bar* 10 μm. c Circuit model describing the relation among fluidic resistances of different flow section in the device

gage pressure ( $P_{\text{drive}} - P_{\text{atm}}$ ) from the device inlet, where  $P_{\text{atm}}$  (defined as the '0' gage pressure) is the atmospheric pressure at the device outlet. To analyze for the flow rates along different parts of the device, we can simplify the device structure as a lumped-circuit model (Fig. 2c), consisting of the fluidic resistances of the confining channel ( $R_{\text{trap}}$ ), bypass microchannels ( $R_{\text{bypass}}$ ) the upstream inlet channel ( $R_{\text{in}}$ ) and the downstream outlet channel ( $R_{\text{out}}$ ). Values of the fluidic resistances have been obtained by commercial simulation software with:  $R_{\text{in}} = 5.2 \times 10^{-5}$ ,  $R_{\text{out}} = 5.2 \times 10^{-5}$ ,  $R_{\text{bypass}} = 10.1 \times 10^{-5}$  MPa s/mm<sup>3</sup>.  $R_{\text{trap}}$  for an empty confining microchannel is  $8.2 \times 10^{-2}$  MPa s/mm<sup>3</sup>, whereas  $R_{\text{trap}}$  should become larger with a cell encapsulated. The fluidic resistance of the entire device ( $R_{\text{device}}$ ) can be approximated as

$$R_{\text{device}} = R_{\text{in}} + R_{\text{out}} + \frac{R_{\text{trap}}R_{\text{bypass}}}{R_{\text{bypass}} + 2R_{\text{trap}}}. \quad (8)$$

Since  $R_{\text{trap}} \gg R_{\text{bypass}}$ ,  $R_{\text{device}} \approx R_{\text{in}} + R_{\text{out}} + R_{\text{bypass}}/2$ , implying that the hydraulic pressure difference across the confining channel can be maintained under a steady driving pressure of the device. On the other hand, it should be mentioned that the gage inlet pressure  $P_{\text{in}}$  used in the computation of  $F_{\text{drag}}(t)$ , as described in Sect. 2, can be obtained by  $P_{\text{in}} = [1 - (R_{\text{in}} + R_{\text{out}})/R_{\text{device}}] \times P_{\text{drive}}$ .

## 4.2 Cell movement along a confining microchannel

To measure the cell viscoelasticity, we first applied a static gas pressure from the device inlet to drive cells into the confining microchannel, in which the cells first contacted the channel side wall and then were squeezed gradually by the sidewalls along their flows along the channel. We had calibrated for the inlet pressure of 0.3 kPa to ensure the cell velocity along the confining channel <30  $\mu\text{m/s}$  after contact, such that the cell shapes and positions could be captured clearly with our imaging system. For the demonstration purpose, representative time-lapsed microscopic images of an MCF-7 cell are shown in Fig. 3a. The distance from the channel entrance where the flowing cell first contacted with the sidewalls was considered as  $x_{\text{contact}}$  as indicated in Fig. 3a); and we considered this moment as the contact time  $t = 0$ . In this study, we consider  $x_{\text{contact}}$  as the position of a contacting cell appeared in the first time-lapsed image, yet a better estimate of  $x_{\text{contact}}$  could be based on  $D_{\text{cell}} \approx W_{\text{out}} + (W_{\text{in}} - W_{\text{out}})x_{\text{contact}}/L_{\text{channel}}$  or with an imaging device with a higher frame rate. It was also observed that each cell gradually moved deeper along the confining channel with a constant confinement angle ( $\theta = 2.48^\circ$ ) but a decreasing velocity after the initial contact (Fig. 3b), indicating clear viscoelastic characteristics of the cell. For every time-lapsed image, we first measured the cell position  $L(t)$ . Considering

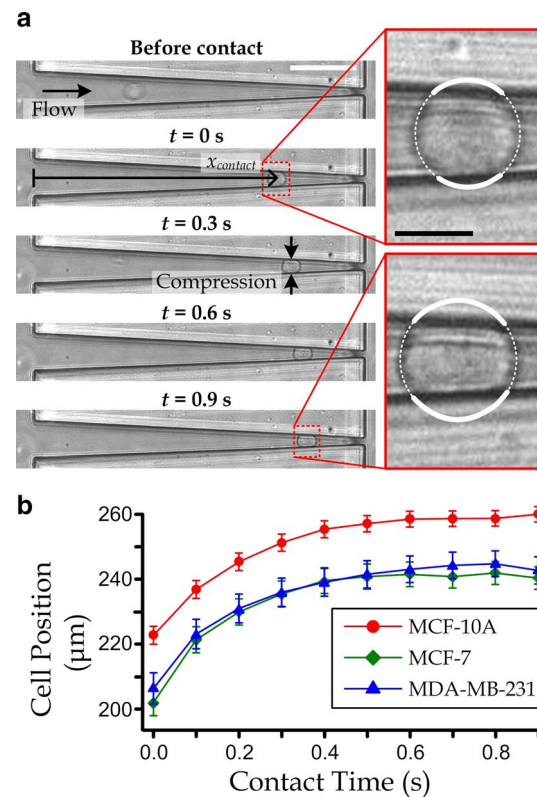


**Fig. 3** **a** Representative snapshots showing the position of a MCF-7 cell flowing along a confining microchannel with deformation due to compression by the channel sidewalls. The initial contact time  $t = 0$  s is defined as the moment of the cell first contact with the sidewalls at the position  $x_{\text{contact}}$ . Scale bar 50  $\mu\text{m}$ . Insets cell shapes at  $t = 0$  s and  $t = 0.9$  s and fitting-circles (white) with the diameter  $D_{\text{deform}}(t)$ . **b** Cell positions of MCF-10A ( $n = 102$ ), MCF-7 ( $n = 87$ ) and MDA-MB-231 ( $n = 89$ ) as functions of contact time with the side walls under a device driving pressure of 0.3 kPa

that observing  $W_{\text{deform}}(t)$  directly from the micrograph would induce an error of the pixel scale ( $\sim 570$  nm/pixel), here we applied the measured  $L(t)$  to calculate  $W_{\text{deform}}(t) = (W_{\text{out}} + (W_{\text{in}} - W_{\text{out}})L(t)/L_{\text{channel}})$  to reduce the measurement error down to  $\sim 50$  nm. We also measured the deformed cell diameter  $D_{\text{deform}}(t)$  for every image. We applied Eq. 1 (i.e.,  $D_{\text{cell}} = [3W_{\text{deform}}(D_{\text{deform}}^2 - W_{\text{deform}}^2/3)/2]^{1/3}$ ) to estimate  $D_{\text{cell}}$  as the average value obtained from the micrograph of a cell right before contacting the sidewalls and the following three time-lapsed images after contact, in order to obtain a better estimate of  $D_{\text{cell}}$ . We then calculated  $F_{\text{drag}}(t)$  at the measured  $D_{\text{cell}}$  and  $L(t)$  by bilinear interpolation (Vadillo-Rodriguez and Dutcher 2009) of the closest representative simulated values shown in Fig. 1c. Based on our results, the average  $D_{\text{cell}}$  of MCF-10A ( $n = 102$ ), MCF-7 ( $n = 87$ ), MDA-MB-231 ( $n = 89$ ) were  $13.39 \pm \text{SE } 0.32$ ,  $16.52 \pm \text{SE } 0.33$  and  $16.99 \pm \text{SE } 0.42$   $\mu\text{m}$ , respectively. We also wrote custom scripts using MATLAB (Mathworks, MA, USA) to implement nonlinear fitting of  $\sigma(t)$  using the Gauss–Newton

algorithm to obtain  $\sigma_o$ ,  $\sigma_s$  and  $\tau$  as described in Eq. 4. More specifically, our results indicate extremely strong correlation coefficients ( $R^2 \sim 1$ ) of the curving fitting for MCF-10A ( $R^2 = 0.994 \pm \text{SD } 0.005$ ), MCF-7 ( $R^2 = 0.991 \pm \text{SD } 0.010$ ) and MDA-MB-231 ( $R^2 = 0.989 \pm \text{SD } 0.024$ ) (Fig. 4). We have proven that  $\sigma(t)$  can be considered as an exponentially stabilizing function as described in Eq. 4; and therefore we can then solve the remaining key viscoelastic parameters  $E_2$  and  $\eta$  using Eqs. 6 and 7, respectively (Fig. 5).

### 4.3 Viscoelastic properties

We further processed the time-lapsed images to analyze for the transient compression stress–strain ratios  $\sigma(t)/\varepsilon(t)$  using Eq. 2 as shown in Fig. 5. We estimated the instantaneous modulus  $E_1$  as the value of  $\sigma(t)/\varepsilon(t)$  at  $t = 0$  using Eq. 3. In practice, we considered the relaxed modulus  $E_s$  as the value of  $\sigma(t)/\varepsilon(t)$  at  $t = 15$  s, which was at least one order of magnitude larger than the time constant  $\tau$ . Based on the measured parameters, we could obtain the whole-cell strain function  $\varepsilon(t)$  using Eq. 5, in which the variable  $E_2$  is substituted with  $E_1 E_2 / (E_1 - E_s)$  according to Eq. 6. Thus, we calculated  $\eta$  for every measurement using Eq. 7.

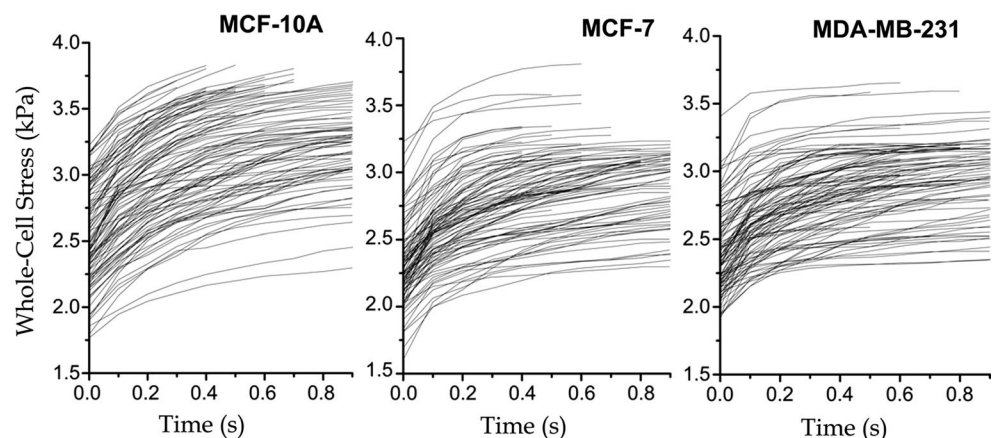
Statistics of the relaxed modulus  $E_s$  and key parameters ( $E_1$ ,  $E_2$  and  $\eta$ ) of the SLS model are listed in Table 1. These results show that the cancer cells MCF-7 and MDA-MB-231 have lower relaxed moduli ( $E_s$ ) than the normal breast cells (MCF-10A); and MDA-MB-231 cells are softer than MCF-7, complying with previous observations by other research groups including Guck et al. (Guck et al. 2005) and Ward et al. (Ward et al. 1991). Likewise, MDA-MB-231 has the largest instantaneous modulus ( $E_1$ ), whereas MCF-10A has the smallest value among the three cell lines. The measured viscosity coefficients ( $\eta$ ) agree with relations reported in the past that the viscosity of MDA-MB-231 > the viscosity of MCF-10A > the viscosity of MCF-7 (Rother et al.

2014). Orders of magnitude of the measured viscosities ( $\eta \sim 1$  kPa s) fell in the same ranges obtained from nanoindentation-based measurements (Bausch et al. 1998; Forgacs et al. 1998; González-Cruz et al. 2012). The correlation coefficients for MCF-10A, MCF-7 and MDA-MB-231 are  $0.968 \pm \text{SD } 0.031$ ,  $0.933 \pm \text{SD } 0.074$  and  $0.923 \pm \text{SD } 0.087$ , respectively; and hence the adopted SLS model is representative for describing the cell viscoelasticity.

Additionally, we have investigated the possible correlations between  $D_{\text{cell}}$ ,  $\eta$ ,  $E_1$  and  $E_2$ , shown in Fig. 6. Apparently,  $D_{\text{cell}}$  and  $\eta$  have no significant correlations with the other biophysical parameters.  $E_1$  should have an inverse correlation with  $E_2$ . By considering the reciprocal moduli (subplot in Fig. 6), we further obtained an inverse linear relationship between  $1/E_1$  and  $1/E_2$  ( $R^2 = 0.531$ , 0.809 and 0.783 for MCF-10A, MCF-7 and MDA-MB-231, respectively).

It has been widely demonstrated that the biophysical properties (e.g., cell rigidity and viscosity) can be considered as independent quantities reflecting the metastatic potentials of cancer cells (Ateshian 2015). Our results in Table 1 agree with the previous research on the correlations between biomechanical and malignant properties of cancer cells. For example, cell types with lower relaxed moduli ( $E_s$ ), i.e., softer, seem to indicate their higher levels of malignant properties and metastatic potentials (Guck et al. 2005; Ward et al. 1991). It has also been reported that the malignant cell MDA-MB-231 has significantly larger viscosity than the less malignant cell MCF-7 and the benign cell MCF-10A (Rother et al. 2014). Importantly, the reported biomechanical phenotyping technique can distinguish malignant cells not only from benign cells but also among different malignant cells types in certain extents. This technique can be further implemented on more cell types for the classification applications.

**Fig. 4** Transient whole-cell stresses of cells flowing through the confining microchannel. Some curves end before the contact time 0.9 s because of the corresponding cells with smaller diameters escaping from the channel. The cell numbers of MCF-10A, MCF-7 and MDA-MB-231 are 102, 87 and 89, respectively



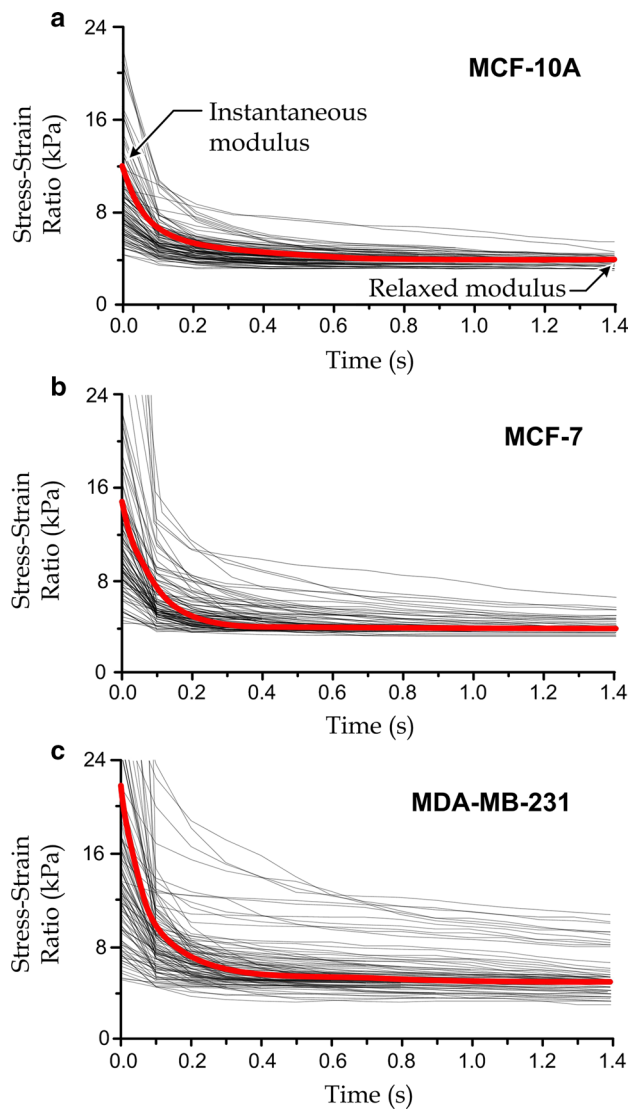


**Fig. 5** Transient stress–strain ratios of MCF-10A, MCF-7 and MDA-MB-231 as for the cells flowing along the confining channel. The *gray lines* describe the transient stress–strain ratios of individual cells. The *red lines* are the nonlinear fits of the mean values at different time points. The cell numbers of MCF-10A, MCF-7 and MDA-MB-231 are 102, 87 and 89, respectively (color figure online)

#### 4.4 Cell-type classification

Based on our measurements, MCF-10A, MCF-7 and MDA-MB231 have significantly different viscoelastic

**Table 1** Measured parameters of the cell viscoelasticity model for the normal and cancerous breast cells

	$E_1$ (kPa)	$E_2$ (kPa)	$E_s$ , or $E_1 E_2 / (E_1 + E_2)$ (kPa)	$\eta$ (kPa s)
MCF-10A	$12.3 \pm \text{SE } 0.7$	$10.0 \pm \text{SE } 1.1$	$4.83 \pm \text{SE } 0.19$	$1.89 \pm \text{SE } 0.21$
MCF-7	$14.5 \pm \text{SE } 1.1^{**}$	$7.0 \pm \text{SE } 0.6^{**}$	$4.21 \pm \text{SE } 0.06^{**}$	$1.64 \pm \text{SE } 0.18^*$
MDA-MB-231	$22.4 \pm \text{SE } 3.2^{**}$	$5.9 \pm \text{SE } 0.3^{**}$	$4.17 \pm \text{SE } 0.06^{**}$	$2.56 \pm \text{SE } 0.38^{**}$

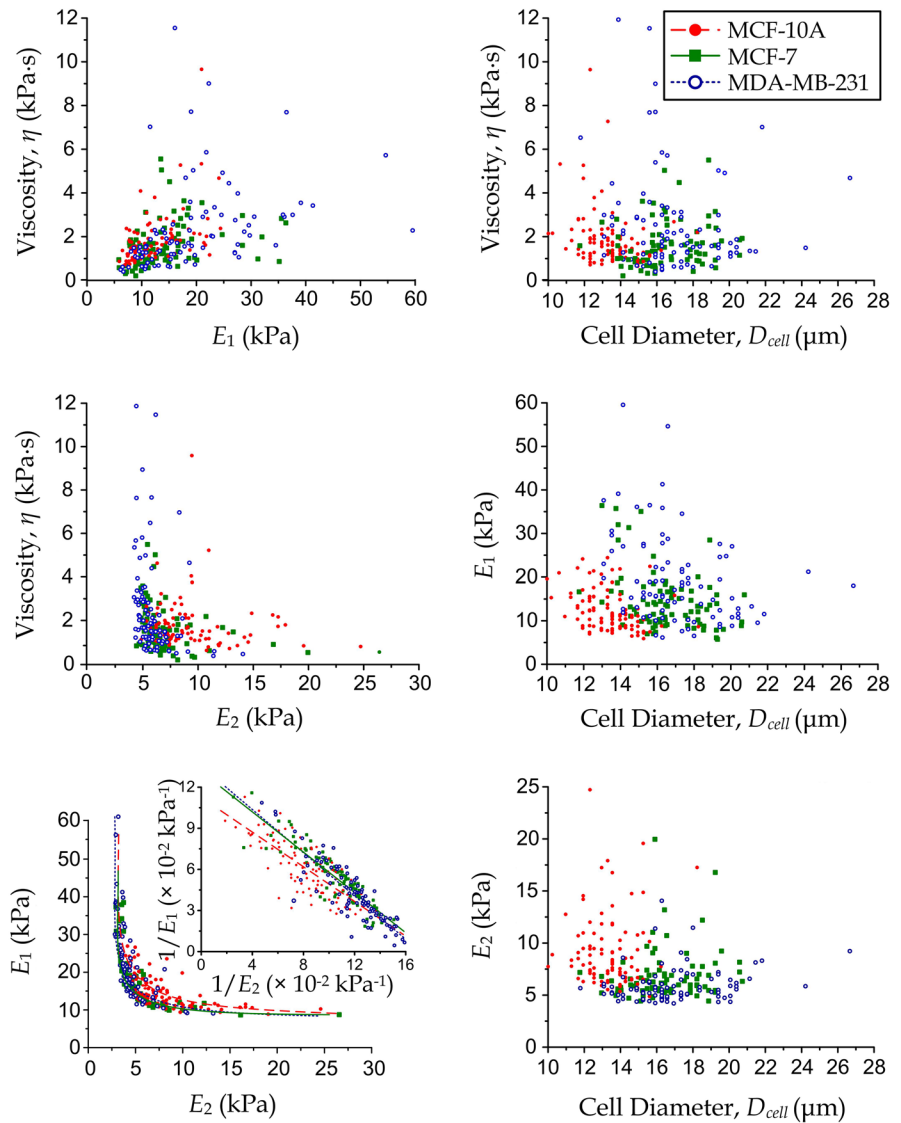
\* Significant differences with  $p$  value  $<0.05$

\*\*  $p$  value  $<0.01$ , comparing to the corresponding case of MCF-10A

properties. We have further attempted to implement classification of cell types based the measured  $D_{\text{cell}}$ ,  $\eta$ ,  $1/E_1$  and  $1/E_2$  as shown in Fig. 7. We first mapped these four biophysical parameters as a two-dimensional scatter plot based on principle component analysis (PCA), a widely adopted approach to efficiently reducing complexity of multiparametric analyses (Tatusov et al. 2001). Experimental data of every cell were projected as a two-dimensional plot by a transformation matrix computed using PCA with average values of the biophysical parameters. We then applied the Quadratic Discriminant Analysis (Friedman 1989) with custom MATLAB scripts to compute the quadratic decision boundaries (*solid lines*), defining the most representative regions for the selected cell types. Our results show the selectivity for every cell type, defined as the percentage of cell population lying in the corresponding decision region: 86.6% for MCF-10A, 65.3% for MCF-7, and 81.7% for MDA-MB-231 (Fig. 7). These results indicate that although we can observe significant differences of cell viscoelastic parameters of cell populations as presented in Table 1, the identification of cell malignance and other properties in the single cell basis is challenging, despite how large the cell populations are tested with. Same as other biophysical and biochemical properties, such limitation is mainly due to the fact that a single phenotypic parameter itself cannot fully reflect the genetic and physiological cell properties, rather than caused by the measurement scheme. Nevertheless, this phenotyping strategy can offer additional viscoelastic parameters of single cells, which can then be considered together with other phenotypic parameters and achieve the comprehensive analysis for the more promising ‘deep phenotyping’ of cancer and other cell analyses.

In fact, we have recently reported the application of antibody-coated channel walls for quantifying surface proteins on cancer cells (Hu et al. 2016). In the future development, we can integrate the viscoelasticity measurement with the multiple confining channels coated with different antibodies and connected in series, in order to achieve the biomechanical and biochemical phenotyping at the single cell level. The more comprehensive cell analysis scheme would provide multiple phenotypic properties of every cell and further improved the cell classification sensitivity for the deep phenotyping applications.

**Fig. 6** Scatter plots between key physical properties of the selected cell types: MCF-10A ( $n = 102$ ), MCF-7 ( $n = 87$ ) and MDA-MB-231 ( $n = 89$ ). *Left column (top to bottom):*  $\eta$  versus  $E_1$ ,  $\eta$  versus  $E_2$ , and  $E_1$  versus  $E_2$  (subplot:  $1/E_1$  vs.  $1/E_2$ ; solid lines are the curve fitting); *right column (top to bottom):*  $\eta$  versus  $D_{cell}$ ,  $E_1$  versus  $D_{cell}$  and  $E_2$  versus  $D_{cell}$



### 5 Conclusion

We report a novel strategy to quantify viscoelasticity of single floating cancer cells using a confining microchannel in this paper. We have applied the Hertz’s and Tatar’s theories and an SLS model to convert transient deformations of cells flowing along the microchannel to key cell viscoelastic properties. We have measured the viscoelastic parameters of normal human breast cells (MCF-10A) and cancerous human breast cells (MCF-7 and MDA-MB-231). Notably, the high correlations ( $R^2 \sim 0.99$ ) of fittings between the measured stress–strain ratios and the viscoelastic parameters indicate that the adopted SLS model is representative for measurements using the microfluidic confining channel. We have successfully classified the chosen cell types based on their biophysical quantities

with reasonable sensitivities (>65%). This research provides a low-cost, label-free, scalable and nondestructive method to quantify comprehensive viscoelastic properties of single floating cells.

Further developments of the confining microchannels should include engineering schemes to avoid simultaneous of multiple cells along the same confining channel, to quantify cell surface protein expressions corresponding to every cell measured in the device, and to achieve parallel operation of multiple channels for a higher throughput. We expect that this microfluidic cell viscoelasticity quantification strategy can be further integrated to provide more comprehensive biomechanical and biochemical cell phenotyping and facilitate the deep phenotyping of rare cells including CTCs, (Bendall and Nolan 2012; Ray 2013) unveiling the precise relationships

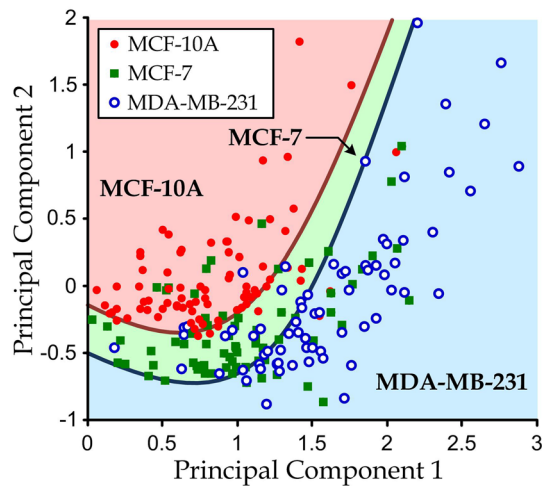


**Fig. 7** Principal component analysis and cell-type classification using biophysical properties of MCF-10A, MCF-7 and MDA-MB-231. The first principle component is  $D_{\text{cell}} + \eta - 1.15 \times 10^{-8}/E_1 + 1.6 \times 10^{-8}/E_2$  and the second principle component is  $-D_{\text{cell}} + 0.00102 \eta + 3.38 \times 10^{-6}/E_1 - 8.8 \times 10^{-6}/E_2$ . The red, green and blue regions are the subspaces for classification of the cell types. The regional boundaries were computed using the ‘quadratic discriminant analysis’ algorithm ( $N > 80$  for every cell type) (color figure online)

between genomic and phenotypic expressions of cancer cells, and thus their potential biological and clinical implications.

**Acknowledgements** We acknowledge financial supports from the National Natural Science Foundation of China (NSFC 31500758), General Research Grant (Project #11206014) and Collaborative Research Fund (Project #C1013-15GF) of Hong Kong Research Grant Council, and the City University of Hong Kong (SRG-Fd 7004540).

## References

- Alix-Panabières C, Pantel K (2013) Circulating tumor cells: liquid biopsy of cancer. *Clin Chem* 59:110–118
- Ateshian GA (2015) Viscoelasticity using reactive constrained solid mixtures. *J Biomech* 48:941–947
- Bao G, Suresh S (2003) Cell and molecular mechanics of biological materials. *Nat Mater* 2:715–725
- Bausch AR, Ziemann F, Boulbitch AA, Jacobson K, Sackmann E (1998) Local measurements of viscoelastic parameters of adherent cell surfaces by magnetic bead microrheometry. *Biophys J* 75:2038–2049
- Bausch AR, Möller W, Sackmann E (1999) Measurement of local viscoelasticity and forces in living cells by magnetic tweezers. *Biophys J* 76:573–579
- Bausch AR, Hellerer U, Essler M, Aepfelbacher M, Sackmann E (2001) Rapid stiffening of integrin receptor-actin linkages in endothelial cells stimulated with thrombin: a magnetic bead microrheology study. *Biophys J* 80:2649–2657
- Bendall SC, Nolan GP (2012) From single cells to deep phenotypes in cancer. *Nat Biotechnol* 30:639–647

- Byun S et al (2013) Characterizing deformability and surface friction of cancer cells. *Proc Natl Acad Sci* 110:7580–7585
- Chaffer CL, Weinberg RA (2011) A perspective on cancer cell metastasis. *Science* 331:1559–1564
- Chambers AF, Groom AC, MacDonald IC (2002) Dissemination and growth of cancer cells in metastatic sites. *Nat Rev Cancer* 2:563–572
- Chawla K, Lee S, Lee BP, Dalsin JL, Messersmith PB, Spencer ND (2009) A novel low-friction surface for biomedical applications: modification of poly (dimethylsiloxane) (PDMS) with polyethylene glycol (PEG)-DOPA-lysine. *J Biomed Mater Res A* 90:742–749
- Chen W et al (2013) Surface-micromachined microfiltration membranes for efficient isolation and functional immunophenotyping of subpopulations of immune cells. *Adv Healthc Mater* 2:965–975
- Cheng L, Xia X, Yu W, Scriven L, Gerberich W (2000) Flat-punch indentation of viscoelastic material. *J Polym Sci Part B: Polym Phys* 38:10–22
- Dudani JS, Gossett DR, Henry T, Di Carlo D (2013) Pinched-flow hydrodynamic stretching of single-cells. *Lab Chip* 13:3728–3734
- Etsion I, Kligerman Y, Kadin Y (2005) Unloading of an elastic-plastic loaded spherical contact. *Int J Solids Struct* 42:3716–3729
- Fletcher DA, Mullins RD (2010) Cell mechanics and the cytoskeleton. *Nature* 463:485–492
- Forgacs G, Foty RA, Shafrir Y, Steinberg MS (1998) Viscoelastic properties of living embryonic tissues: a quantitative study. *Biophys J* 74:2227–2234
- Friedman JH (1989) Regularized discriminant analysis. *J Am Stat Assoc* 84:165–175
- Fung Y-C (2013) *Biomechanics: mechanical properties of living tissues*. Springer Science & Business Media, Berlin
- Gittes F, MacKintosh F (1998) Dynamic shear modulus of a semiflexible polymer network. *Phys Rev E* 58:R1241
- González-Cruz RD, Fonseca VC, Darling EM (2012) Cellular mechanical properties reflect the differentiation potential of adipose-derived mesenchymal stem cells. *Proc Natl Acad Sci* 109:E1523–E1529
- Gossett DR et al (2012) Hydrodynamic stretching of single cells for large population mechanical phenotyping. *Proc Natl Acad Sci* 109:7630–7635
- Guck J et al (2005) Optical deformability as an inherent cell marker for testing malignant transformation and metastatic competence. *Biophys J* 88:3689–3698
- Hoffman BD, Grashoff C, Schwartz MA (2011) Dynamic molecular processes mediate cellular mechanotransduction. *Nature* 475:316–323
- Hohne DN, Younger JG, Solomon MJ (2009) Flexible microfluidic device for mechanical property characterization of soft viscoelastic solids such as bacterial biofilms. *Langmuir* 25:7743–7751
- Hu S, Liu G, Chen W, Li X, Lu W, Lam RH, Fu J (2016) Multiparametric biomechanical and biochemical phenotypic profiling of single cancer cells using an elasticity microcytometer. *Small* 12:2300–2311
- Huang S-B et al (2013) High-purity and label-free isolation of circulating tumor cells (CTCs) in a microfluidic platform by using optically-induced-dielectrophoretic (ODEP) force. *Lab Chip* 13:1371–1383
- Hur SC, Henderson-MacLennan NK, McCabe ER, Di Carlo D (2011) Deformability-based cell classification and enrichment using inertial microfluidics. *Lab Chip* 11:912–920
- Inglis DW, Riehn R, Austin R, Sturm J (2004) Continuous microfluidic immunomagnetic cell separation. *Appl Phys Lett* 85:5093–5095

- Ketene AN, Schmelz EM, Roberts PC, Agah M (2012) The effects of cancer progression on the viscoelasticity of ovarian cell cytoskeleton structures. *Nanomed: Nanotechnol Biol Med* 8:93–102
- Kim D-H, Wong PK, Park J, Levchenko A, Sun Y (2009) Microengineered platforms for cell mechanobiology. *Annu Rev Biomed Eng* 11:203–233
- Kong TF et al (2015) Enhancing malaria diagnosis through microfluidic cell enrichment and magnetic resonance relaxometry detection. *Sci Rep* 5:11425–11436
- Lei KF, Butt YK (2010) Colorimetric immunoassay chip based on gold nanoparticles and gold enhancement. *Microfluid Nanofluid* 8:131–137
- Lei KF, Wu M-H, Liao P-Y, Chen Y-M, Pan T-M (2012) Development of a micro-scale perfusion 3D cell culture biochip with an incorporated electrical impedance measurement scheme for the quantification of cell number in a 3D cell culture construct. *Microfluid Nanofluid* 12:117–125
- Lekka M et al (2012) Cancer cell recognition—mechanical phenotype. *Micron* 43:1259–1266
- Li S, Patwardhan AG, Amirouche FM, Havey R, Meade KP (1995) Limitations of the standard linear solid model of intervertebral discs subject to prolonged loading and low-frequency vibration in axial compression. *J Biomech* 28:779–790
- Li P et al (2015) Acoustic separation of circulating tumor cells. *Proc Natl Acad Sci* 112:4970–4975
- Lin Y-H, Wang C-C, Lei KF (2014) Bubble-driven mixer integrated with a microfluidic bead-based ELISA for rapid bladder cancer biomarker detection. *Biomed Microdev* 16:199–207
- Liu K-K (2006) Deformation behaviour of soft particles: a review. *J Phys D Appl Phys* 39:R189
- Liu K, Williams D, Briscoe B (1998) The large deformation of a single micro-elastomeric sphere. *J Phys D Appl Phys* 31:294
- Liu Z, Fu X, Binks BP, Shum HC (2015) Mechanical compression to characterize the robustness of liquid marbles. *Langmuir* 31:11236–11242
- Luo Y et al (2014) A constriction channel based microfluidic system enabling continuous characterization of cellular instantaneous Young's modulus. *Sens Actuators B: Chem* 202:1183–1189
- Maheswaran S et al (2008) Detection of mutations in EGFR in circulating lung-cancer cells. *N Engl J Med* 359:366–377
- Moendarbary E et al (2013) The cytoplasm of living cells behaves as a poroelastic material. *Nat Mater* 12:253–261
- Nagrath S et al (2007) Isolation of rare circulating tumour cells in cancer patients by microchip technology. *Nature* 450:1235–1239
- Ray LB (2013) Cells go solo. *Science* 342:1187
- Rother J, Nöding H, Mey I, Janshoff A (2014) Atomic force microscopy-based microrheology reveals significant differences in the viscoelastic response between malign and benign cell lines. *Open Biol* 4:140046
- Shevde LA, Welch DR (2003) Metastasis suppressor pathways—an evolving paradigm. *Cancer Lett* 198:1–20
- Sollier E et al (2014) Size-selective collection of circulating tumor cells using Vortex technology. *Lab Chip* 14:63–77
- Steeg PS (2006) Tumor metastasis: mechanistic insights and clinical challenges. *Nat Med* 12:895–904
- Suresh S (2007) Biomechanics and biophysics of cancer cells. *Acta Mater* 55:3989–4014
- Swaminathan V, Mythreye K, O'Brien ET, Berchuck A, Blobe GC, Superfine R (2011) Mechanical stiffness grades metastatic potential in patient tumor cells and in cancer cell lines. *Can Res* 71:5075–5080
- Tan SC, Pan WX, Ma G, Cai N, Leong KW, Liao K (2008) Viscoelastic behaviour of human mesenchymal stem cells. *BMC Cell Biol* 9:1
- Tatusov RL et al (2001) The COG database: new developments in phylogenetic classification of proteins from complete genomes. *Nucleic Acids Res* 29:22–28
- Tran QD, Kong TF, Hu D, Marcos M, Lam RH (2016) Deterministic sequential isolation of floating cancer cells under continuous flow. *Lab Chip* 16:2813–2819
- Trickey WR, Baaijens FP, Laursen TA, Alexopoulos LG, Guilak F (2006) Determination of the Poisson's ratio of the cell: recovery properties of chondrocytes after release from complete micropipette aspiration. *J Biomech* 39:78–87
- Vadillo-Rodriguez V, Dutcher JR (2009) Dynamic viscoelastic behavior of individual Gram-negative bacterial cells. *Soft Matter* 5:5012–5019
- Wang MM et al (2005) Microfluidic sorting of mammalian cells by optical force switching. *Nat Biotechnol* 23:83–87
- Wang Z, Kim M-C, Marquez M, Thorsen T (2007) High-density microfluidic arrays for cell cytotoxicity analysis. *Lab Chip* 7:740–745
- Ward KA, Li WI, Zimmer S, Davis T (1991) Viscoelastic properties of transformed cells: role in tumor cell progression and metastasis formation. *Biorheology* 28:301–313
- Warren K, Mpagazehe J, LeDuc P, Higgs C III (2016) Geometric effects in microfluidics on heterogeneous cell stress using an Eulerian-Lagrangian approach. *Lab Chip* 16:593–598
- Wu Y, McEwen GD, Harihar S, Baker SM, DeWald DB, Zhou A (2010) BRMS1 expression alters the ultrastructural, biomechanical and biochemical properties of MDA-MB-435 human breast carcinoma cells: an AFM and Raman microspectroscopy study. *Cancer Lett* 293:82–91
- Xia Y, Whitesides GM (1998) Soft lithography. *Ann Rev Mater Sci* 28:153–184
- Yang T et al (2015) An integrated optofluidic device for single-cell sorting driven by mechanical properties. *Lab Chip* 15:1262–1266
- Zhang Z, Kristiansen H, Liu J (2007) A method for determining elastic properties of micron-sized polymer particles by using flat punch test. *Comput Mater Sci* 39:305–314
- Zhang W et al (2012) Microfluidics separation reveals the stem-cell-like deformability of tumor-initiating cells. *Proc Natl Acad Sci* 109:18707–18712